Focal mechanisms of small earthquakes beneath the whole Japan Islands based on first-motion polarities picked using deep learning

Takahiko Uchide[1,*]

[1] Geological Survey of Japan, National Institute of Advanced Industrial Science and Technology (AIST)

Abbreviated Title: Focal Mechanisms in the Whole Japan Islands

* Corresponding Author: Takahiko Uchide (t.uchide@aist.go.jp)

Summary

Knowledge of crustal stress field is essential for understanding tectonics and earthquake generation. One way to estimate the crustal stress field is based on focal mechanisms of earthquakes. This study investigated focal mechanisms of ~ 110 thousand microearthquakes in Japan Islands shallower than 20 km based on the first-motion polarities picked by a simple neural network model, which was trained using two data sets: moderate to large earthquakes all over Japan and microearthquakes in two regions in Japan. The threshold of the confidence score from the neural network model was so chosen as to maximize the overall quality of focal mechanism solutions. The P- and T-axes of the numerous focal mechanism solutions provide more detailed distributions of crustal stress field. For example, in Chugoku region, there exist slight differences in the trend of P-axes azimuths between the northern and southern areas are observed, corresponding to the geodetic observations in space.

Keywords

- Earthquake source observations
- Seismicity and tectonics
- Neural networks, fuzzy logic

1. Introduction

Crustal stress field data are crucial to understand tectonics and seismic activity; however, measuring it at depths over a wide area is a challenge. Direct measurements at specific boreholes (e.g., Wu *et al.* 2007, Huffman *et al.* 2016, Brodsky *et al.* 2017, Townend *et al.* 2017) offer detailed information but only for one point. In contrast, seismology provides indirect measurements with more uncertainty but for a wide area. The focal mechanisms, which indicate the directions of fault plane and slip, indicate the orientation of the seismogenic stress. The World Stress Map (Heidbach *et al.* 2008, Heidbach *et al.* 2016, Heidbach *et al.* 2018) compiles this information all over the world.

In the past, routinely determined moment tensor solutions were used for estimating regional stress fields (Terakawa and Matsu'ura 2010, Hardebeck 2015). However, blank areas still exist even in seismically active area such as Japan Islands. More complete knowledge of the seismogenic stress field requires focal mechanisms of microearthquakes, especially in low seismicity areas (e.g., Imanishi *et al.* 2011, Imanishi *et al.* 2012, Matsumoto *et al.* 2015). Comprehensive investigations of microearthquake focal mechanisms reveal the regional stress field (e.g., Iio *et al.* 2018, Imanishi *et al.* 2019).

The focal mechanisms of moderate or larger earthquakes can be automatically determined using the full waveform from the local (e.g., Dreger and Helmberger 1993, Fukuyama *et al.* 1998) or global seismic network (e.g., Ekström *et al.* 2012). However, the mechanisms of small earthquakes cannot be similarly determined because of the difficulty of modeling high-frequency seismograms. We usually use the first-motion polarity: the vertical component initially goes either upward or downward. Automatic polarity-picking methods, such as one based on the sign of the first extremum after the P

arrival (Nakamura 2004, Chen and Holland 2016). Pugh *et al.* (2016a) proposed a Bayesian approach using the first extremum and a probability function of P arrival time. Recently, deep learning has enabled us to automatically pick the polarity (Ross *et al.* 2018, Hara *et al.* 2019). Thus, we are technically ready to investigate large number of microearthquakes.

The aim of this study was to obtain the focal mechanism solutions in Japan Islands, one of the most seismically active regions in the world. The first-motion polarities were picked using a neural network model and seismic data from nationwide seismic networks. Finally, the focal mechanism solutions and spatial trends in P- and T-axes were studied.

2. Training the Neural Network Model

2.1. Data

The training of the neural network model was performed in two stages. In the first stage, the Hi-net data of 18,000 earthquakes with P arrival and polarity data in the JMA catalog were used. Most of these earthquakes are larger than *M* 3 (Fig. S1). The whole data were then spatially divides into the training and validation data sets (Fig. 1a, Table 1).

In the second stage, I used the P arrival time and polarity of microearthquakes in Kanto and Chugoku regions, manually picked by Geological Survey of Japan, National Institute of Advanced Industrial Science and Technology (AIST). The Kanto data were used by Imanishi *et al.* (2019). The spatial distributions of used events in Kanto and Chugoku regions are shown in Figs. 1b and 1c, respectively. The number of seismogram sets and earthquakes is summarized in Table 1.

In the both stages, seismograms of three components (up-down, north-south, and east-west) were used. Each component had 256 samples: 156 samples before and 100 samples after P arrival. The samples are 2.56-s long, as the data were sampled at 100 Hz. Low-frequency noise was removed by applying a high-pass filter at 1 Hz. I emphasized the initial portion of the P-wave by clipping seismograms at a certain threshold.

Furthermore, I augmented the data four times by flipping all three components, rotating horizontal components by randomly selected angles, and time-shifting. The flipping procedure equalizes the number of positive and negative polarity data. The time shift addresses potential misalignment of data due to uncertainties in the arrival time picking.

Later, I examined various values of the clipping threshold and the time-shift range.

2.2. Design of the Neural Network Model

Fig. 2 summarizes the neural network used in this study. The input of the neural network models is a three-component 256-sample long seismogram set where the 156th sample corresponds to the P-arrival time already picked either manually or automatically. The output comprises two scores corresponding to the upward and downward polarities. Note that, in the case of Southern California, Ross *et al.* (2018) classified the polarity as "Up," "Down," and "Unknown"; however, in this study, the "Unknown" class is not set. The data set contained many seismograms with impulsive onset but no polarity information (e.g., Fig. S2), and the lack of polarity information does not mean "Unknown" in this case.

I designed a simple neural network model (Fig. 2) similar to the ones used in prior studies (Ross *et al.* 2018, Hara *et al.* 2019). The neural network model started with two

convolution layers, followed by three units composed of convolution, batch-normalization (Ioffe and Szegedy 2015), and pooling layers. The models ended with two fully connected layers. The kernel size of the convolutional layers was 11. For all but the final layers, the activation function was the Rectified Linear Units (ReLU) (Nair and Hinton 2010); SoftMax function was chosen for the final layer:

$$\mathrm{softmax}(\mathbf{z})_i = \frac{\exp(z_i)}{\sum_j \exp(z_j)}, \quad (1)$$

where $\mathbf{z} = (z_1, z_2)$ is the output of the final layer corresponding to the positive and negative polarities, respectively. Then, the outputs are non-negative, and their summation is always 1. In order to address the overfitting problem, the dropout technique (Srivastava *et al.* 2014) was adopted: 50 % of randomly selected perceptions were muted during the training. The loss was evaluated by the negative log-likelihood function and the parameters of the neural network model were updated by back-propagating the loss (Rumelhart *et al.* 1986) optimized by the adaptive moment estimation (Adam) method (Kingma and Ba 2014).

2.3. Result

Hundred cases with randomly selected clipping thresholds in the range of 10^{-6} to 10^{-4} m/s and the half-width of the time-shift ranging 0–30 samples were examined. The result was evaluated based on the loss value for the test data set. The result shows that the shorter half-width of the time-shift range, the smaller is the loss (Fig. 3a). The clipping threshold has no correlation with the loss value (Fig. 3b).

Hereafter, I did not apply time-shift and used 10^{-5} m/s as the clipping threshold. The neural network model was trained using these values. The precision-recall curve of the

trained model is shown in Fig. 3c.

3. Application to Crustal Earthquakes in Japan

I applied the trained model to event data of earthquakes that occurred in the period 2005–2019 at depths less than 20 km within the coastline, excluding the events for which polarity information is already available in the catalog (Table 1). I used seismograms from Hi-net and the JMA seismic network with P-wave arrival times in the JMA catalog. Preprocessing was done in the same way as the training. Good results were obtained for polarity picking with high scores (Fig. 4), even in noisy cases.

The focal mechanisms were determined using polarity information with scores larger than a confidence threshold and the HASH code (Hardebeck and Shearer 2002, 2008). The quality of focal mechanisms depends on the confidence threshold (Fig. 3d). If the threshold is too high, the very small number of polarity picks cannot constrain focal mechanisms well. If the threshold is lower than 0.7, the fraction of A and B ranks given by the HASH code (Hardebeck and Shearer 2008) is almost constant. I adopted a confidence threshold of 0.7.

Fig. 5 shows the estimated focal mechanisms and their P- and T- axes in addition to the NIED F-net Moment Tensor solutions for reference. The focal mechanisms of 113,700 events are estimated, while those of 6830 events are undetermined because the number of stations was smaller than 8. Ranks A, B, C, and D by the HASH code (Hardebeck and Shearer 2008) were given to 1060, 17890, 36958, and 50962 events, respectively. The focal mechanism solutions cover much more space than those in a routine catalog.

The obtained P- and T-axes (Figs. 5c and 5d, respectively) are well consistent with stress regimes reported in prior studies: north-south extensional stress field in Kyushu region (Matsumoto *et al.* 2015, Savage *et al.* 2016); normal faulting earthquakes in the area of Fukushima-Hamadori and northern Ibaraki prefecture (Imanishi *et al.* 2012).

4. Discussion

It may be surprising that the narrower time-shift range of the data, the better is the model performance, because the time-shifting would make the model more flexible and robust to uncertainties in arrival time picking. There are two potential reasons. One is that the arrival times in the test data were accurate because of careful review by an analyst, and therefore the time-shift was not really required. Another possible reason is the shortage of training data from microearthquakes.

Determination of focal mechanisms from the first-motion polarities of P-waves picked by the trained neural network model is also important for assessing the quality of polarity picking. In this study 50.8 % of the focal mechanism solutions are ranked D or undetermined. In a study on the determination of the focal mechanisms of earthquakes in Southern California using manually picked P-wave polarity and the amplitude ratio of P and S waves (Yang *et al.* 2012), the results showed that 56.6 % (101,309 out of 178,899 events) of the events were ranked D, comparable to the result of this study. Thus, this study yields a reasonable quality of the P-wave first-motion polarity picking, though the comparison is not simple because of many factors including the differences in the observational conditions such as the magnitude range and station density. Focal mechanism determination can be improved in several ways: introduction of P-wave

157 amplitude (e.g., Matsushita and Imanishi 2015, Pugh *et al.* 2016b) and the ratio of P- and
158 S-wave amplitudes (Hardebeck and Shearer 2003, Yang *et al.* 2012), as well as the
159 advances in the P-wave polarity picking.

160 The quality of the focal mechanism solutions is shown by region in Fig. 3e. In particular,
161 the quality in Hokkaido region is much worse than in other regions. The reason was
162 examined by focusing on the number of stations. First, the quality of the focal mechanism
163 solutions is well correlated with the number of stations (Fig. 3f). Next, the number of
164 usable stations is smaller in Hokkaido than in other regions. This is probably because of
165 the spatial density of seismic stations (Fig. 5e). Hence, it is more difficult to determine
166 the focal mechanisms in Hokkaido than elsewhere.

167 We see interesting features in the spatial distribution of the P- and T-axis azimuths (Figs.
168 5c and 5d). For example, in Chugoku region, the P-axes strike in the east–west direction
169 in the northern area (San-in area), whereas those strike in the NW–SE direction in the
170 southern one (Sanyo area). The contrast in the P-axis azimuths in western Tottori was
171 reported by Kawanishi *et al.* (2009). This study too shows a similar trend over the whole
172 Chugoku region. This contrast geographically corresponds to the San-in shear zone
173 (Meneses-Gutierrez and Nishimura 2020). A combination of this study with geodetic
174 implications will enhance our understanding of seismotectonics.

175 In spite of the dramatic increase in focal mechanism solutions, there are still blank areas
176 in Japan Islands. The seismicity is quite low in such areas. Hence, this kind of study may
177 need to be performed even for smaller earthquakes, which is a greater challenge than that
178 tackled in the present study. Additional campaign seismic observations may improve the
179 focal mechanism solutions of very small earthquakes. In addition, combining these

observations with various observations including geological, geographical, and geodetical ones will improve our understanding of the crustal stress field and its origin.

5. Conclusions

In this study, the focal mechanisms of small to microearthquakes are estimated for better understanding of the crustal stress fields in Japan Islands. The focal mechanisms were derived using the P-wave first-motion polarities picked by a neural network model that takes three-component seismograms with P arrival times as the input. The focal mechanisms of almost all microearthquakes over the whole of Japan Islands were successfully determined. The focal mechanism solutions are generally consistent with the stress regime on a large scale. The slight but clear differences in the P-axis azimuths in the northern and southern parts of Chugoku region are consistent with the geodetic observations for this region. The results of this study will be useful for revealing the crustal stress field, and thus, for assessing the past and current tectonic activities and future earthquake generation.

Acknowledgements

I thank Kazutoshi Imanishi and Reiken Matsushita for providing phase data for microearthquakes in Kanto and Chugoku regions in Japan. I also thank the NIED, especially Takanori Matsuzawa, for helping me prepare the large seismic data set. I used seismic data from NIED Hi-net (National Research Institute for Earth Science and Disaster Resilience 2020) and JMA available at http://www.hinet.bosai.go.jp/?LANG=en (last accessed on 25 March 2020), the phase data from JMA Unified Earthquake Catalog, available at http://www.data.jma.go.jp/svd/eqev/data/bulletin/eqdoc_e.html (last

accessed on 25 March 2020) and http://www.hinet.bosai.go.jp/?LANG=en (last accessed on 25 March 2020), and the moment tensor solutions by NIED F-net project (Fukuyama *et al.* 1998) available at http://www.fnet.bosai.go.jp/top.php?LANG=en (last accessed on 25 March 2020). The data analyses in this study were performed using PyTorch (Paszke *et al.* 2019), ObsPy (Beyreuther *et al.* 2010, Megies *et al.* 2011, Krischer *et al.* 2015), HASH (Hardebeck and Shearer 2002, 2008), and HASHpy (Williams 2014). I used Generic Mapping Tools (Wessel *et al.* 2013) for generating Figs. 1, 3, 5, and S1, and Matplotlib (Hunter 2007) for Figs. 4 and S2. This work was supported by Mitsubishi Foundation and AIST EDGE Runners project. In this work, the computation facility of the AI Bridging Cloud Infrastructure (ABCI) maintained by AIST was employed.

References

Amante, C. & Eakins, B.W., 2009. ETOPO1 1 Arc-Minute Global Relief Model: Procedures, Data Sources and Analysis. *in NOAA Technical Memorandum NESDIS NGDC-24*National Geophysical Data Center, NOAA, doi:10.7289/V5C8276M.

Beyreuther, M., Barsch, R., Krischer, L., Megies, T., Behr, Y. & Wassermann, J., 2010. ObsPy: A Python Toolbox for Seismology, *Seismol. Res. Lett.,* 81**,** 530-533, doi:10.1785/gssrl.81.3.530.

Brodsky, E.E., Saffer, D., Fulton, P., Chester, F., Conin, M., Huffman, K., Moore, J.C. & Wu, H.-Y., 2017. The postearthquake stress state on the Tohoku megathrust as constrained by reanalysis of the JFAST breakout data, *Geophys. Res. Lett.,* 44**,** 8294-8302, doi:10.1002/2017gl074027.

Chen, C. & Holland, A.A., 2016. PhasePApy: A Robust Pure Python Package for

225 Automatic Identification of Seismic Phases, *Seismol. Res. Lett.,* 87**,** 1384-1396,
226 doi:10.1785/0220160019.
227 Dreger, D.S. & Helmberger, D.V., 1993. Determination of source parameters at regional
228 distances with three-component sparse network data, *J. Geophys. Res.,* 98**,** 8107-
229 8125, doi:10.1029/93JB00023.
230 Ekström, G., Nettles, M. & Dziewoński, A.M., 2012. The global CMT project 2004–
231 2010: Centroid-moment tensors for 13,017 earthquakes, *Phys. Earth Plant. Inter.,*
232 200–201**,** 1-9, doi:10.1016/j.pepi.2012.04.002.
233 Fukuyama, E., Ishida, M., Dreger, D.S. & Kawai, H., 1998. Automated seismic moment
234 tensor determination by using on-line broadband seismic waveforms, *Zisin 2nd*
235 *Ser.,* 51**,** 149-156, doi:10.4294/zisin1948.51.1_149. (*in Japanese with English*
236 *abstract*)
237 Hara, S., Fukahata, Y. & Iio, Y., 2019. P-wave first-motion polarity determination of
238 waveform data in western Japan using deep learning, *Earth Planets Space,* 71**,**
239 127, doi:10.1186/s40623-019-1111-x.
240 Hardebeck, J.L., 2015. Stress orientations in subduction zones and the strength of
241 subduction megathrust faults, *Science,* 349**,** 1213-1216,
242 doi:10.1126/science.aac5625.
243 Hardebeck, J.L. & Shearer, P.M., 2002. A new method for determining first-motion focal
244 mechanisms, *Bull. Seismol. Soc. Am.,* 92**,** 2264-2276.
245 Hardebeck, J.L. & Shearer, P.M., 2003. Using S/P amplitude ratios to constrain the focal
246 mechanisms of small earthquakes, *Bull. Seismol. Soc. Am.,* 93**,** 2434-2444.
247 Hardebeck, J.L. & Shearer, P.M., 2008. HASH: A FORTRAN program for computing
248 earthquake first-motion focal mechanisms – v1.2 –.

249 Heidbach, O., Rajabi, M., Cui, X., Fuchs, K., Müller, B., Reinecker, J., Reiter, K., Tingay,
250 M., Wenzel, F., Xie, F., Ziegler, M.O., Zoback, M.-L. & Zoback, M., 2018. The
251 World Stress Map database release 2016: Crustal stress pattern across scales,
252 *Tectonophysics,* 744**,** 484-498, doi:10.1016/j.tecto.2018.07.007.
253 Heidbach, O., Rajabi, M., Reiter, K., Ziegler, M. & Team, W., 2016. World Stress Map
254 Database Release 2016. *in GFZ Data Services*, doi:10.5880/WSM.2016.001.
255 Heidbach, O., Tingay, M., Barth, A., Reinecker, J., Kurfeß, D. & Müller, B., 2008. The
256 World Stress Map database release 2008, doi:10.1594/GFZ.WSM.Rel2008.
257 Huffman, K.A., Saffer, D.M. & Dugan, B., 2016. In situ stress magnitude and rock
258 strength in the Nankai accretionary complex: a novel approach using paired
259 constraints from downhole data in two wells, *Earth Planets Space,* 68**,** 123,
260 doi:10.1186/s40623-016-0491-4.
261 Hunter, J.D., 2007. Matplotlib: A 2D Graphics Environment, *Comput. Sci. Eng.,* 9**,** 90-95,
262 doi:10.1109/MCSE.2007.55.
263 Iio, Y., Kishimoto, S., Nakao, S., Miura, T., Yoneda, I., Sawada, M. & Katao, H., 2018.
264 Extremely weak fault planes: An estimate of focal mechanisms from stationary
265 seismic activity in the San'in district, Japan, *Tectonophysics,* 723**,** 136-148,
266 doi:10.1016/j.tecto.2017.12.007.
267 Imanishi, K., Ando, R. & Kuwahara, Y., 2012. Unusual shallow normal-faulting
268 earthquake sequence in compressional northeast Japan activated after the 2011 off
269 the Pacific coast of Tohoku earthquake, *Geophys. Res. Lett.,* 39**,** L09306,
270 doi:10.1029/2012GL051491.
271 Imanishi, K., Kuwahara, Y., Takeda, T., Mizuno, T., Ito, H., Ito, K., Wada, H. & Haryu,
272 Y., 2011. Depth-dependent stress field in and around the Atotsugawa fault, central

Japan, deduced from microearthquake focal mechanisms: Evidence for localized aseismic deformation in the downward extension of the fault, *J. Geophys. Res.,* 116**,** B01305, doi:10.1029/2010JB007900.

Imanishi, K., Uchide, T., Ohtani, M., Matsushita, R. & Nakai, M., 2019. Construction of the crustal stress map in the Kanto region, central Japan, *Bull. Geol. Surv. Jpn.,* 70**,** 273-298. (*in Japanese with English abstract*)

Ioffe, S. & Szegedy, C., 2015. Batch normalization: accelerating deep network training by reducing internal covariate shift. *in ArXiv e-prints*.

Kawanishi, R., Iio, Y., Yukutake, Y., Shibutani, T. & Katao, H., 2009. Local stress concentration in the seismic belt along the Japan Sea coast inferred from precise focal mechanisms: Implications for the stress accumulation process on intraplate earthquake faults, *J. Geophys. Res. Solid Earth,* 114, doi:10.1029/2008jb005765.

Kingma, D.P. & Ba, J., 2014. Adam: A method for stochastic optimization, *arXiv preprint arXiv:1412.6980*.

Krischer, L., Megies, T., Barsch, R., Beyreuther, M., Lecocq, T., Caudron, C. & Wassermann, J., 2015. ObsPy: a bridge for seismology into the scientific Python ecosystem, *Comput. Sci. Discov.,* 8, doi:10.1088/1749-4699/8/1/014003.

Matsumoto, S., Nakao, S., Ohkura, T., Miyazaki, M., Shimizu, H., Abe, Y., Inoue, H., Nakamoto, M., Yoshikawa, S. & Yamashita, Y., 2015. Spatial heterogeneities in tectonic stress in Kyushu, Japan and their relation to a major shear zone, *Earth Planets Space,* 67**,** 172, doi:10.1186/s40623-015-0342-8.

Matsushita, R. & Imanishi, K., 2015. Stress fields in and around metropolitan Osaka, Japan, deduced from microearthquake focal mechanisms, *Tectonophysics,* 642**,** 46-57, doi:10.1016/j.tecto.2014.12.011.

297 Megies, T., Beyreuther, M., Barsch, R., Krischer, L. & Wassermann, J., 2011. ObsPy –
298 What can it do for data centers and observatories?, *Ann. Geophys.,* 54**,** 12,
299 doi:10.4401/ag-4838.
300 Meneses-Gutierrez, A. & Nishimura, T., 2020. Inelastic deformation zone in the lower
301 crust for the San-in Shear Zone, Southwest Japan, as observed by a dense GNSS
302 network, *Earth Planets Space,* 72**,** 10, doi:10.1186/s40623-020-1138-z.
303 Nair, V. & Hinton, G.E., 2010. Rectified linear units improve restricted boltzmann
304 machines. *in 27th International Conference on Machine Learning (ICML-10)*, pp.
305 807-814, Haifa, Israel.
306 Nakamura, M., 2004. Automatic determination of focal mechanism solutions using initial
307 motion polarities of P and S waves, *Phys. Earth Plant. Inter.,* 146**,** 531-549,
308 doi:10.1016/j.pepi.2004.05.009.
309 National Research Institute for Earth Science and Disaster Resilience, 2020. NIED Hi-
310 net, ed National Research Institute for Earth Science and Disaster Resilience.
311 doi:10.17598/NIED.0003.
312 Paszke, A., Gross, S., Massa, F., Lerer, A., Bradbury, J., Chanan, G., Killeen, T., Lin, Z.,
313 Gimelshein, N., Antiga, L., Desmaison, A., Kopf, A., Yang, E., DeVito, Z., Raison,
314 M., Tejani, A., Chilamkurthy, S., Steiner, B., Fang, L., Bai, J. & Chintala, S., 2019.
315 PyTorch: An imperative style, high-performance deep learning library. *in*
316 *Advances in Neural Information Processing Systems*, pp. 8024-8035Curran
317 Associates, Inc.
318 Pugh, D.J., White, R.S. & Christie, P.A.F., 2016a. Automatic Bayesian polarity
319 determination, *Geophys. J. Int.,* 206**,** 275-291, doi:10.1093/gji/ggw146.
320 Pugh, D.J., White, R.S. & Christie, P.A.F., 2016b. A Bayesian method for microseismic

source inversion, *Geophys. J. Int.*, doi:10.1093/gji/ggw186.

Ross, Z.E., Meier, M.-A. & Hauksson, E., 2018. P wave arrival picking and first-motion polarity determination with deep learning, *J. Geophys. Res. Solid Earth,* 123**,** 5120-5129, doi:10.1029/2017JB015251.

Rumelhart, D.E., Hinton, G.E. & Williams, R.J., 1986. Learning representations by back-propagating errors, *Nature,* 323**,** 533-536, doi:10.1038/323533a0.

Savage, M.K., Aoki, Y., Unglert, K., Ohkura, T., Umakoshi, K., Shimizu, H., Iguchi, M., Tameguri, T., Ohminato, T. & Mori, J., 2016. Stress, strain rate and anisotropy in Kyushu, Japan, *Earth Planet. Sci. Lett.,* 439**,** 129-142, doi:10.1016/j.epsl.2016.01.005.

Shearer, P.M., Prieto, G.A. & Hauksson, E., 2006. Comprehensive analysis of earthquake source spectra in Southern California, *J. Geophys. Res.,* 111**,** B06303, doi:10.1029/2005JB003979.

Srivastava, N., Hinton, G., Krizhevsky, A., Sutskever, I. & Salakhutdinov, R., 2014. Dropout: a simple way to prevent neural networks from overfitting, *J. Mach. Learn. Res.,* 15**,** 1929-1958.

Terakawa, T. & Matsu'ura, M., 2010. The 3-D tectonic stress fields in and around Japan inverted from centroid moment tensor data of seismic events, *Tectonics,* 29**,** TC6008, doi:10.1029/2009TC002626.

Townend, J., Sutherland, R., Toy, V.G., Doan, M.-L., Célérier, B., Massiot, C., Coussens, J., Jeppson, T., Janku-Capova, L., Remaud, L., Upton, P., Schmitt, D.R., Pezard, P., Williams, J., Allen, M.J., Baratin, L.-M., Barth, N., Becroft, L., Boese, C.M., Boulton, C., Broderick, N., Carpenter, B., Chamberlain, C.J., Cooper, A., Coutts, A., Cox, S.C., Craw, L., Eccles, J.D., Faulkner, D., Grieve, J., Grochowski, J.,

345 Gulley, A., Hartog, A., Henry, G., Howarth, J., Jacobs, K., Kato, N., Keys, S.,
346 Kirilova, M., Kometani, Y., Langridge, R., Lin, W., Little, T., Lukacs, A., Mallyon,
347 D., Mariani, E., Mathewson, L., Melosh, B., Menzies, C., Moore, J., Morales, L.,
348 Mori, H., Niemeijer, A., Nishikawa, O., Nitsch, O., Paris, J., Prior, D.J., Sauer, K.,
349 Savage, M.K., Schleicher, A., Shigematsu, N., Taylor-Offord, S., Teagle, D.,
350 Tobin, H., Valdez, R., Weaver, K., Wiersberg, T. & Zimmer, M., 2017.
351 Petrophysical, Geochemical, and Hydrological Evidence for Extensive Fracture-
352 Mediated Fluid and Heat Transport in the Alpine Fault's Hanging-Wall Damage
353 Zone, *Geochem. Geophys. Geosyst.,* 18**,** 4709-4732, doi:10.1002/2017GC007202.
354 Wessel, P., Smith, W.H.F., Scharroo, R., Luis, J. & Wobbe, F., 2013. Generic Mapping
355 Tools: Improved Version Released, *EOS,* 94**,** 409-410,
356 doi:10.1002/2013eo450001.
357 Williams, M.C., 2014. HASHpy, doi:10.5281/zenodo.9808.
358 Wu, H.-Y., Ma, K.-F., Zoback, M., Boness, N., Ito, H., Hung, J.-H. & Hickman, S., 2007.
359 Stress orientations of Taiwan Chelungpu-Fault Drilling Project (TCDP) hole-A as
360 observed from geophysical logs, *Geophys. Res. Lett.,* 34,
361 doi:10.1029/2006gl028050.
362 Yang, W., Hauksson, E. & Shearer, P.M., 2012. Computing a large refined catalog of focal
363 mechanisms for southern California (1981–2010): Temporal stability of the style
364 of faulting, *Bull. Seismol. Soc. Am.,* 102**,** 1179-1194, doi:10.1785/0120110311.
365

366

Tables

Table 1

Numbers of seismograms and earthquakes contained in data sets.

Region	Type of Data Set	Seismogram Sets	Earthquakes
All Japan	Training	279,483	17,402
	Validation	7,666	598
Kanto	Training	12,814	1,262
	Validation	784	56
	Test	1,483	113
Chugoku	Training	63,359	2,259
	Validation	7,674	322
	Test	12,838	595
All Japan	Application	1,930,132	113,700

Figures

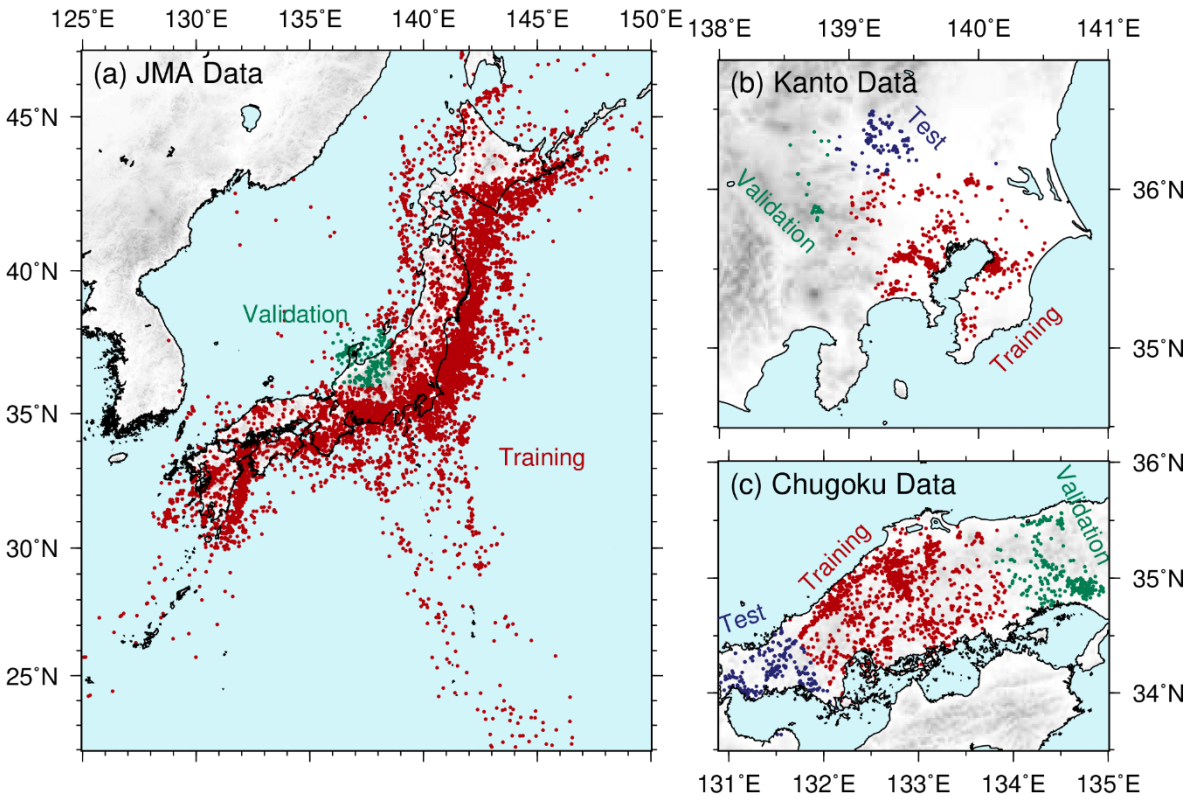

Fig. 1

Distribution of the epicentres of the earthquakes used for training (red), validation (green), and testing (blue) of the neural network model. Topography is from ETOPO1 (Amante and Eakins 2009).

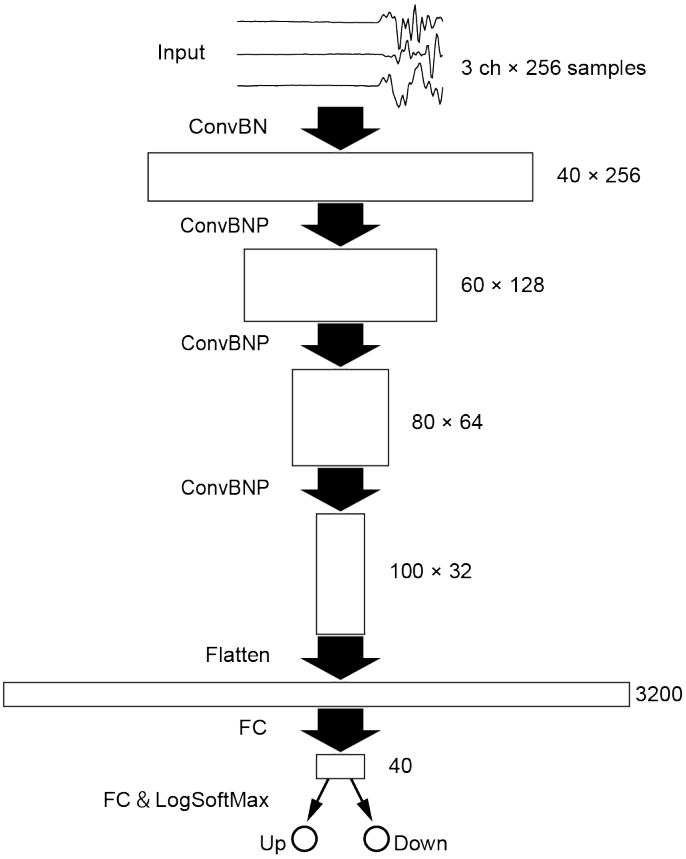

Fig. 2

Design of the neural network model. Numbers on the right indicate the number of channels and samples. "ConvBN," "Conv BNP," and "FC" denote convolution and batch normalization layers; convolution, batch normalization, and pooling layers; and fully connected layers, respectively.

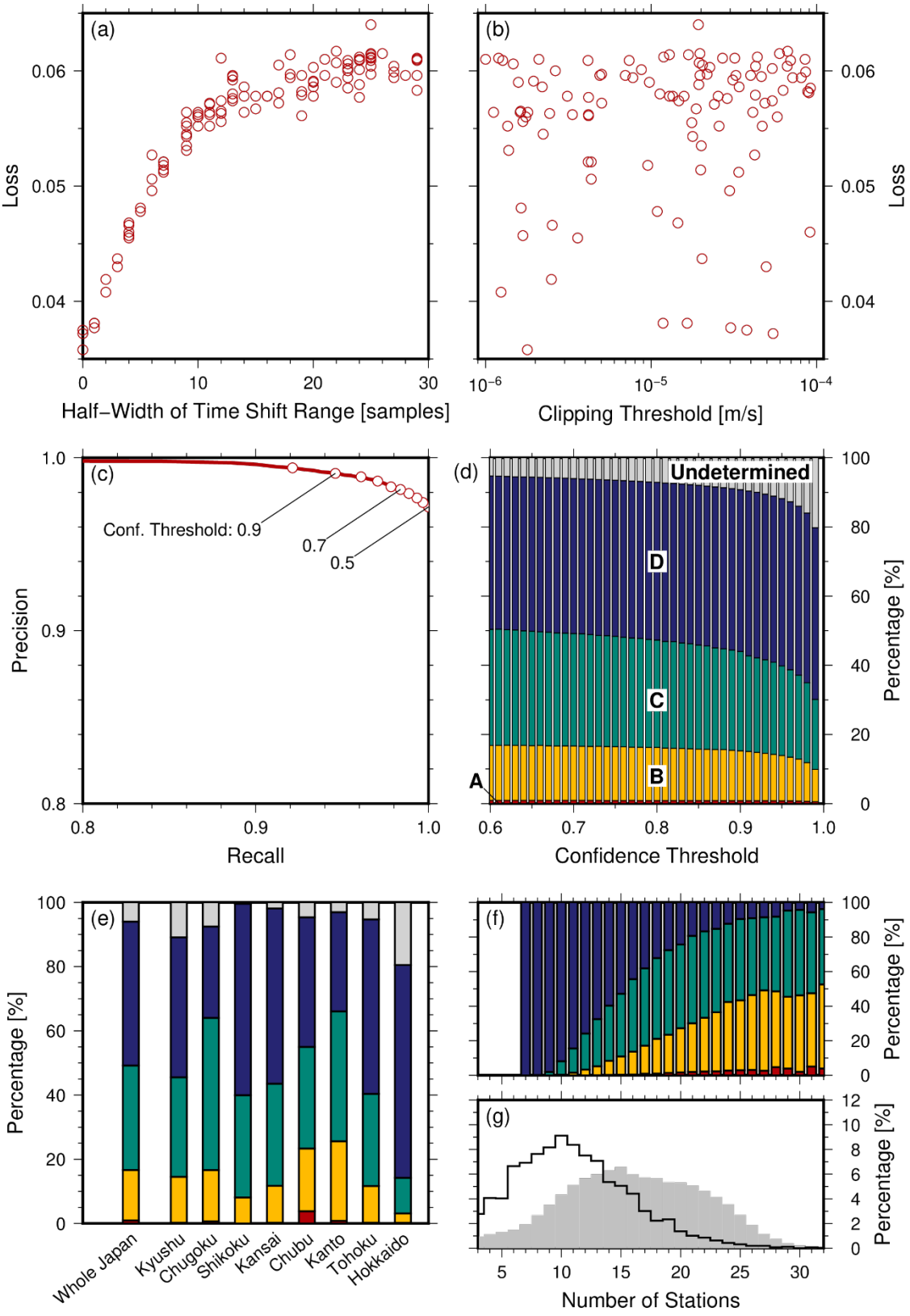
(a)
Loss
0.06
0.05
0.04
0
10
20
30
Half−Width of Time Shift Range [samples]
(b)
Loss
0.06
0.05
0.04
10^{-6}
10^{-5}
10^{-4}
Clipping Threshold [m/s]
(c)
Precision
1.0
0.9
0.8
Conf. Threshold: 0.9
0.7
0.5
0.8
0.9
1.0
Recall
(d)
Undetermined
D
C
B
A
Percentage [%]
100
80
60
40
20
0
0.6
0.7
0.8
0.9
1.0
Confidence Threshold
(e)
Percentage [%]
100
80
60
40
20
0
Whole Japan
Kyushu
Chugoku
Shikoku
Kansai
Chubu
Kanto
Tohoku
Hokkaido
(f)
Percentage [%]
100
80
60
40
20
0
(g)
Percentage [%]
12
10
8
6
4
2
0
5
10
15
20
25
30
Number of Stations

383

Fig. 3

Summary of the results. Here, (a) and (b) show the loss function values as functions of the time-shift range and the clipping threshold, respectively. (c) Precision-recall curve of the trained model for the test data set. Circles correspond to every 0.05 units of the confidence thresholds. (d) Bar graphs of the rank of focal mechanism solutions as a function of the confidence threshold. (e) Bar graphs of the rank of focal mechanism solutions for the whole of Japan and eight regions. Here a model with a confidence threshold of 0.7 was used. (f) Bar graphs as a function of the number of stations. (g) Histograms of events as a function of the number of stations. The black line and gray shaded region indicate the values for Hokkaido and other regions, respectively.

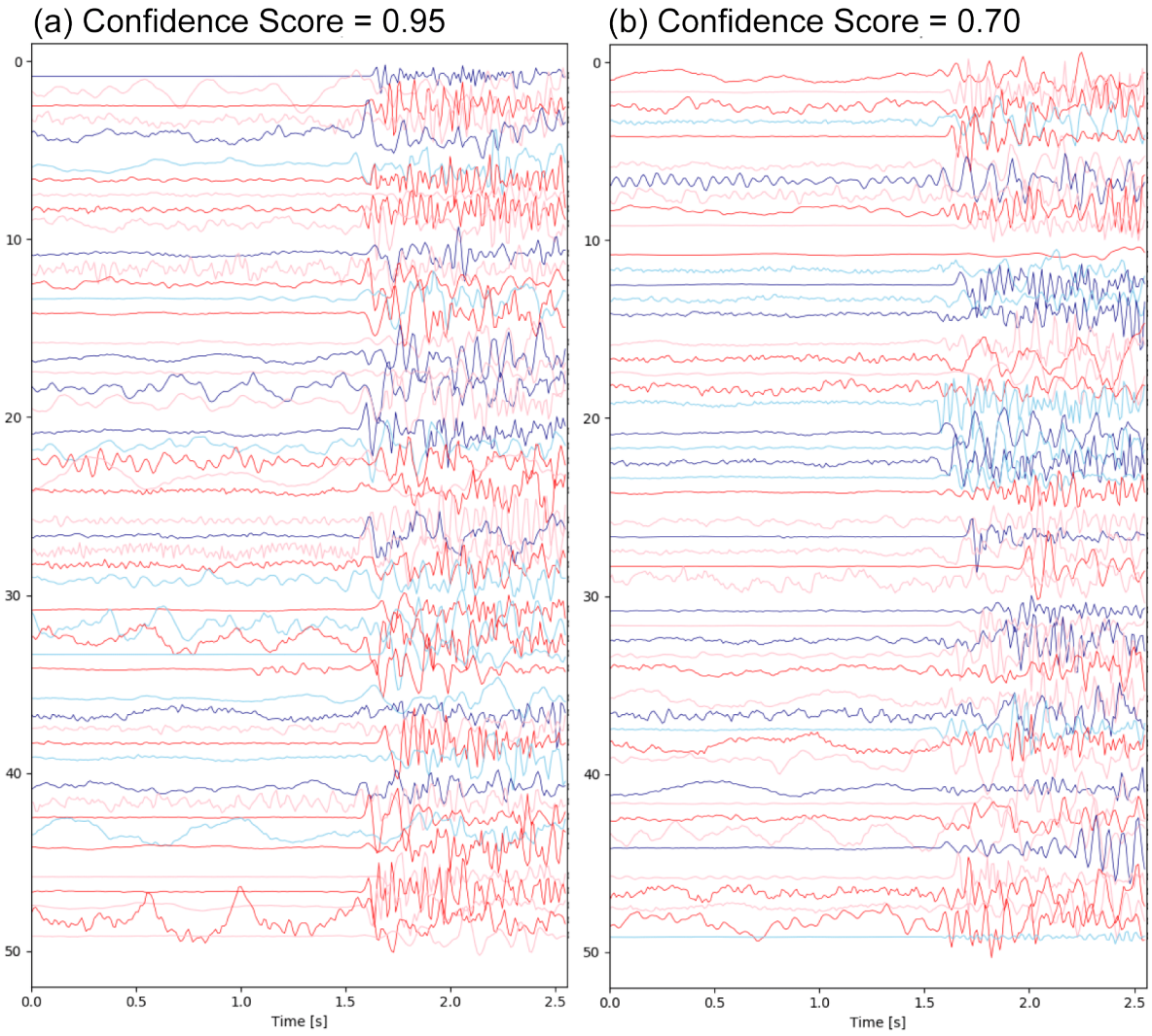

Fig. 4

Examples of polarities picked by the neural network model with confidence scores of (a) 0.95 and (b) 0.70. Seismograms with negative polarities are flipped. If correctly picked, the first motion looks positive in this figure. Light and dark colors are alternatively for convenience.

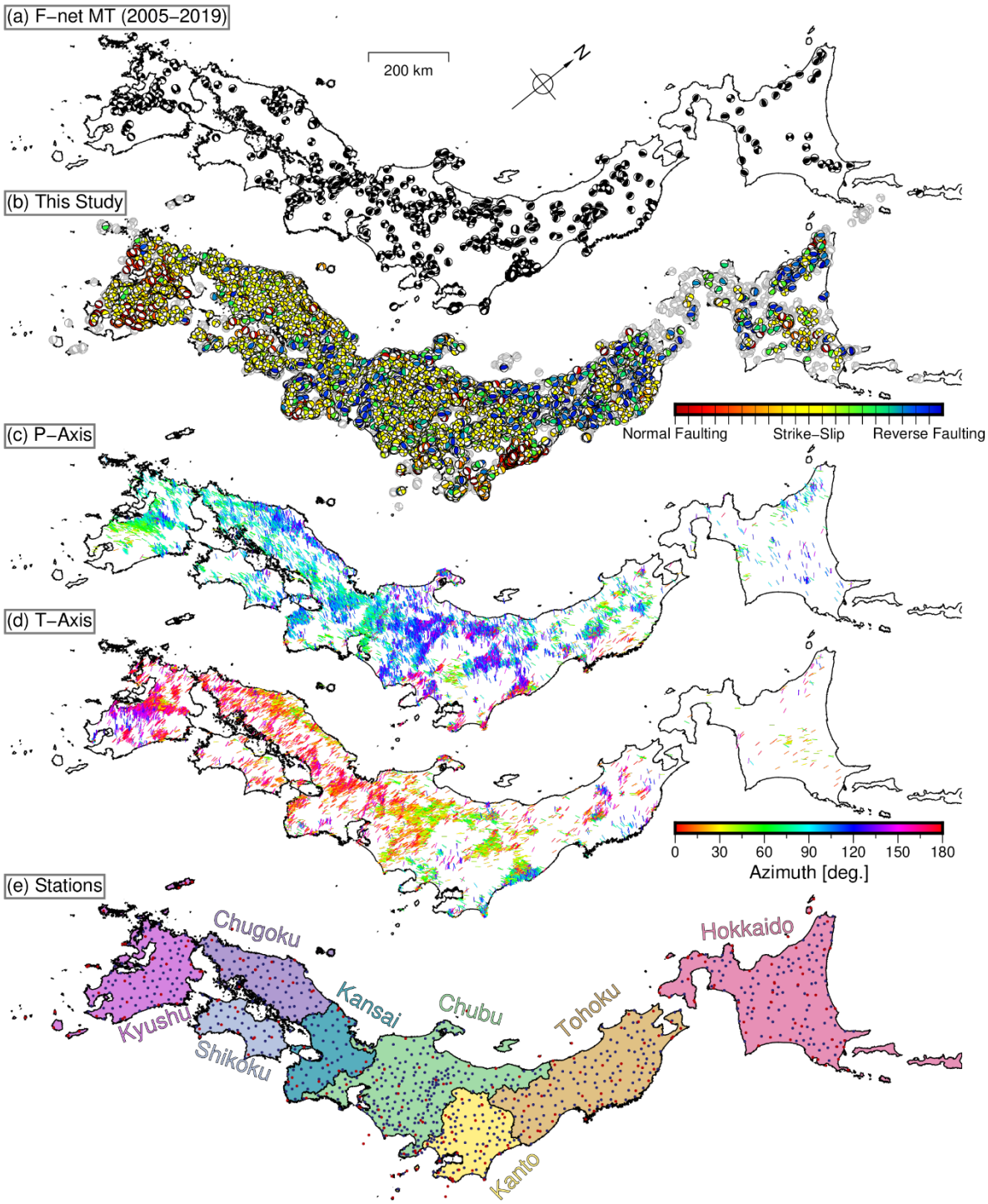

Fig. 5

(a) Moment tensor solutions of earthquakes in 2006-2019 by NIED F-net Project (Fukuyama *et al.* 1998), for reference. (b) Focal mechanism solutions in this study. Solutions ranked A–C (Hardebeck and Shearer 2008) are colored according to focal

405 mechanism types (Shearer *et al.* 2006). Solution ranked D are shown by gray beach balls.
406 (c) Azimuths of the P-axes of the estimated focal mechanism solutions ranked A – C and
407 with less than 30° of plunge. Colors indicate the azimuths. (d) Azimuths of the T-axes. (e)
408 Station distribution.